RSC Advances

PAPER

View Article Online
View Journal | View Issue

Cite this: *RSC Adv.*, 2026, **16**, 6890

Microstructurally optimizing the mid-infrared optical modulation properties of vanadium oxide thin films *via* magnetron sputtering and subsequent annealing

Sen Jin,[ab] Ningning Dong,*[ab] Zhouyuan Yan,[ab] Jincheng Ji,[ab] Weihao Yu[abc] and Jun Wang*[ab]

Vanadium dioxide (VO_2) is a promising material for mid-infrared optical modulation due to its reversible metal-insulator transition. This study presents an efficient and stable method for fabricating VO_2 thin films with enhanced optical limiting performance *via* crystallinity control and microstructural optimization. The process combines magnetron sputtering with gradient annealing, and the effects of annealing temperature on film structure and optical properties were analyzed using X-ray diffraction, X-ray spectroscopy, and SEM. Annealing at 550 °C yielded high-quality monoclinic $VO_2(M_1)$ films with excellent crystallinity, low defect density, and island-like grains (250–300 nm). The optimized film showed reduced oxygen vacancies (17.3%) and increased V^{4+} content. Optical measurements revealed strong thermal switching: mid-infrared transmittance dropped from 85% at 25 °C to 35% at 80 °C, achieving a 50% modulation depth—12.5-fold higher than that of unannealed films. Under 3.8 μm laser irradiation, modulation depth tripled. The annealing process effectively improved phase purity and reduced defects by encouraging grain growth and oxygen vacancy repair. This work provides key insights into the structure–defect–property relationships in VO_2 and offers a scalable route for producing high-performance phase-change oxide thin films.

Received 7th December 2025
Accepted 26th January 2026

DOI: 10.1039/d5ra09458e

rsc.li/rsc-advances

1 Introduction

High-power lasers with excellent directionality and ultra-high power density are developing rapidly.[1] These devices incapacitate targets through instantaneous thermal and radiation-induced optical damage mechanisms, posing threats to both human vision and photoelectric detection equipment.[2,3] The urgent need for defenses against has driven extensive research into optical limiting materials capable of providing effective optical modulation while maintaining high transmittance under low-intensity laser irradiation.[4–7] Phase-change materials have emerged as promising candidates for this type of adaptive optical modulation. These materials maintain high transparency under low-intensity laser irradiation but automatically attenuate high-power laser radiation through increased reflectance and absorption *via* phase transition.[8–11]

Vanadium dioxide (VO_2) is the most widely studied of such phase-change materials. Its transformation between monoclinic semiconducting and rutile metallic phases occurs at ~68 °C, inducing dramatic optical property modulation that provides a unique combination of broadband spectral response and self-activated protection mechanisms. This positions VO_2 as an ideal material for next-generation intelligent optical modulation systems.[12–14] The investigation of VO_2 for use in laser protection applications entered its new stage in the 1990s through pioneering research on VO_2/V_2O_3 composite films for photodetector safeguarding.[15] Recent research focusing on designing asymmetric nonlinear optical protection devices and metasurface optical limiters based on VO_2 has effectively achieved strong laser suppression with high modulation ratios and broadband asymmetric transmission in the mid-infrared range.[16,17] Parallel advances in related research include investigations into femtosecond laser-induced optical property modifications and mechanisms in VO_2 films[18] as well as innovative fabrication processes that enhance film uniformity and adhesion.[19–21] Additionally, self-excited VO_2 films have been developed for use in anti-laser applications and exhibit rapid responses to high-power laser threats.[22,23] These collective advances have established the fundamental technical foundations necessary for the large-scale implementation of VO_2 films in optical modulation systems.

[a]*Optoelectronics & Interdisciplinary Department, Shanghai Institute of Optics and Fine Mechanics, Chinese Academy of Sciences, Shanghai 201800, China. E-mail: n.n.dong@siom.ac.cn*

[b]*Center of Materials Science and Optoelectronics Engineering, University of Chinese Academy of Sciences, Beijing 100049, China*

[c]*Hangzhou Institute for Advanced Study, University of Chinese Academy of Sciences, Hangzhou, 310024, China*

Current techniques for fabricating VO_2 films include magnetron sputtering, sol–gel processing, pulsed laser deposition, and chemical vapor deposition.[24–33] These preparation methods have their own advantages. For instance, VO_2 thin films fabricated by magnetron sputtering exhibit low phase purity, often containing vanadium oxides of other valence states, but are suitable for large-area preparation. In contrast, films grown by pulsed laser deposition (PLD) demonstrate high cleanliness and excellent crystallinity, though they are not suitable for large-scale production. However, critical challenges limit the implementation of these methods: first, the multivalent nature of vanadium enables the formation of multiple oxides (VO, V_2O_3, V_6O_{13}, V_2O_5), requiring precise stoichiometric control; second, VO_2 itself exhibits polymorphism with various crystalline phases including VO_2(R), VO_2(M_1), VO_2(M_2), VO_2(A), VO_2(B), VO_2(C), VO_2(D), and VO_2(T),[34–36] each of which exhibits a distinct electronic band structure, phase transition temperature, infrared transmittance/modulation behavior, density, specific heat capacity, and thermal conductivity.[37–43] CThe surface coverage, density, and microstonsequently, stoichiometric ratios must be precisely controlled to prevent the formation of competing vanadium oxides, which imposes stringent requirements on process stability. Furthermore, challenges associated with the application of VO_2 films in laser protect applications include insufficient room-temperature transmittance and inadequate modulation contrast between high- and low-temperature phases.

This study addressed these challenges and limitations by applying magnetron sputtering followed by thermochemical conversion *via* annealing treatment to fabricate VO_2 thin films. Notably, directly utilizing a VO_2 target as the sputtering source mitigated the multivalent state issue while enhancing crystallinity and optimizing film morphology through controlled post-processing. The resulting film demonstrated exceptional performance with a mid-infrared transmittance reaching 85% at room temperature and a modulation depth of ~50% at 80 °C, representing an approximately 12.5-fold improvement over that of a non-annealed film. Furthermore, the 3.8 μm optical limiting performance of the annealed VO_2 film was three times greater than that of a non-annealed film. Thus, this study demonstrated an efficient and cost-effective strategy for fabricating VO_2 thin films, paving the way for their practical implementation in mid-infrared optical modulation systems.

2 Experimental materials and methods

2.1 Film fabrication

The VO_x films evaluated in this study were fabricated using a two-step method comprising magnetron sputtering followed

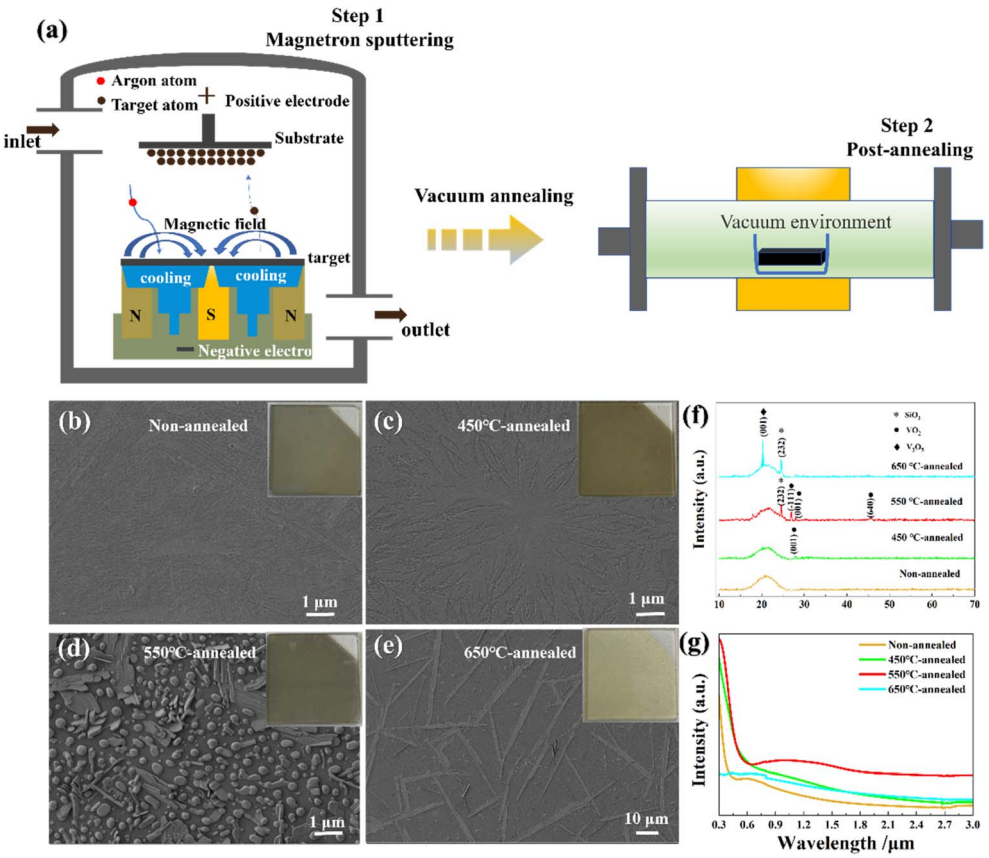

Fig. 1 (a) Schematic of the proposed method for preparing VO_X films. SEM images and photographs (inset) of the (b) non-annealed, (c) 450 °C annealed, (d) 550 °C annealed, and (e) 650 °C annealed film specimens. (f) XRD patterns and (g) UV-Vis-NIR patterns of the VO_X films prepared using different annealing temperatures.

by thermochemical conversion *via* vacuum annealing (Fig. 1(a)). All film specimens evaluated in this research were deposited onto quartz substrates by a DC magnetron sputtering system (KYKY JD-500) using a high-purity VO_2 target (99.9%, φ 75 × 3 mm). Each quartz substrate was ultrasonically cleaned for 15 min each in acetone, ethanol, and then deionized water, and subsequently subjected to nitrogen drying. Prior to film deposition, the magnetron chamber was evacuated to a base pressure $<5 \times 10^{-4}$ Pa, then a high-purity argon sputtering gas (99.99%, 60 sccm) was introduced to maintain a working pressure of 0.5 Pa. The sputtering process comprised 15 min of pre-sputtering at 120 W to remove surface contaminants from the target, followed by 20 min of formal deposition onto the substrate, which was heated to 60 °C. Post-deposition annealing was conducted in a tube furnace under an argon atmosphere (50 sccm) using a heating rate of 10 °C min^{-1}. Four film specimens were prepared using identical deposition parameters but different annealing conditions comprising no annealing (as-deposited) and annealing at 450 °C, 550 °C, or 650 °C for 2 h. The resulting film thicknesses were 40 nm, 40 nm, 60 nm, and 12 nm, corresponding to progressively increasing annealing temperatures (Fig. S1–S4), and the surface roughness of the samples is shown in Fig. S5.

2.2 Analysis

The film thickness was measured using a step profiler (Bruker Dektak XT). The surface topography, thickness, and roughness were analyzed by atomic force microscopy (AFM, Bruker Dimension Icon) operated in tapping mode. The morphology was examined using scanning electron microscopy (SEM, Hitachi S-4800II). The phase composition and crystallinity of each specimen were analyzed by X-ray diffraction (XRD, Cu Kα radiation, λ = 1.5406 Å) using a scan rate of 2°/min. The elemental composition and chemical state of each specimen were evaluated by X-ray photoelectron spectroscopy (XPS) using an Escalab 250Xi photoelectron spectrometer (Thermo Fisher Scientific); all binding energies were referenced to the C 1s peak (284.6 eV) arising from adventitious hydrocarbons. Each specimen was also subjected to Fourier transform infrared (FTIR) spectroscopy using a Cary 670 spectrometer (Varian) and ultraviolet, visible, and near infrared (UV-Vis-NIR) absorption spectroscopy using a Cary 5000 spectrophotometer (Varian). Finally, the 3.8 μm laser-induced optical modulation performance of each specimen was evaluated using a custom-built optical limiting test system.

3 Results and discussion

3.1 Film characterization

Fig. 1(b–e) present SEM images of the VO_X thin films prepared using different annealing temperatures; distinct morphologies can be observed across the specimens.

The non-annealed (as-deposited) specimen shown in Fig. 1(b) exhibited a dense but rough surface with small grains and apparent intergranular porosity. The specimen annealed at 450 °C exhibited smoother initial grains but numerous micrometer-scale cracks (Fig. 1(c)); this phenomenon was caused by thermally induced atomic rearrangement during annealing, which promoted grain coarsening and reorientation that reduced interfacial defects, whereas the accompanying grain boundary sliding and stress inhomogeneity induced crack formation. When the annealing temperature was increased to 550 °C (Fig. 1(d)), an island-like growth pattern emerged that was characterized by uniformly distributed islands of VO_2 (250–300 nm in diameter) with localized melting features. This indicates interfacial energy minimization through the coalescence of smaller crystallites. Note that abnormal grain growth was triggered when the annealing temperature was increased further to 650 °C (Fig. 1(e)), forming elongated lamellar structures (widths on the order of several micrometers and lengths extending to several tens of micrometers) with extensive substrate exposure. The formation of these structures likely involved recrystallization processes and extensive melting.[44] The surface coverage, density, and microstructural gaps in VO_2 films evolve systematically with annealing conditions, collectively governing their optical and thermal responses. A continuous and dense film morphology facilitates in-plane heat conduction; however, high defect density and grain boundary scattering can significantly suppress phase transition cooperativity and optical transmittance. When annealing yields a uniform island-like structure with regular nanoscale gaps, low scattering loss, efficient interfacial thermal coupling, and rapid cooperative phase transition within isolated grains can be simultaneously achieved. In contrast, annealing induces abnormal grain growth and discrete micrometer-scale lamellar structures exposes large area of the substrate and creates wide trenches. This morphology results in strong light scattering, impedes lateral heat transport, and degrades the uniformity and response speed of the phase transition. Therefore, by tailoring the annealing-induced microstructure and gap architecture, the performance of VO_2 films in light management, heat conduction, and phase transition dynamics can be selectively optimized, providing a crucial structural basis for their functional design in various optoelectronic applications.

The XRD patterns also indicate structural changes as the annealing temperature increased (Fig. 1(f)). The non-annealed film exhibited no distinct peaks in the 10–70° range, indicating an amorphous or ultrafine-grained structure (grain size < 5 nm) consistent with the disordered lattice typical of low-temperature sputtered films.[45] The specimen annealed at 450 °C exhibited a weak diffraction peak at $2\theta = 27.8°$, matching the (011) plane of the monoclinic $VO_2(M_1)$ phase, reflecting enhanced crystallinity and grain growth. The specimen annealed at 550 °C exhibited additional prominent peaks at 26.9° and 45.6°, which correspond to the (−111) and (640) planes of monoclinic $VO_2(M_1)$, respectively (PDF#09-0142, $P2_1/c$ space group: a = 0.574 nm, b = 0.452 nm, c = 0.538 nm, β = 122.61°).[46] However, annealing at 650 °C eliminated this peak and introduced a strong peak at $2\theta = 20.3°$ which corresponding to the (001) plane of orthorhombic V_2O_5 (PDF#41-1426), confirming a structural phase transition from $VO_2(M_1)$ to thermodynamically stable V_2O_5.[47]

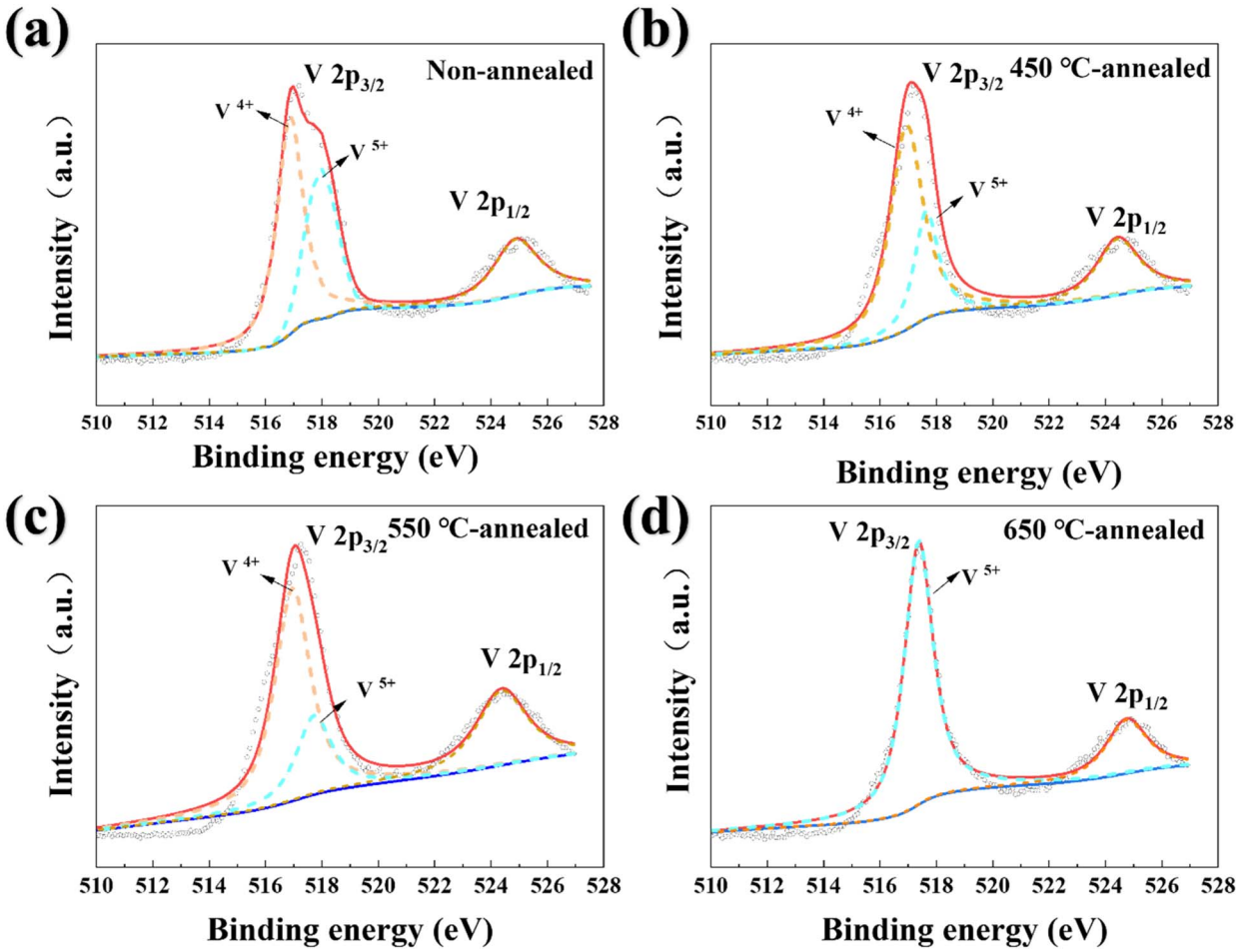

Fig. 2 V 2p XPS patterns of the: (a) non-annealed, (b) 450 °C annealed, (c) 550 °C annealed, and (d) 650 °C annealed VO_2 thin film specimens.

The UV-Vis-NIR absorption spectra indicate annealing-dependent optical absorption behaviors (Fig. 1(g)). The non-annealed, 450 °C annealed, and 550 °C annealed films exhibited similar absorption behaviors with different absorption intensities and a redshift in the resonance peaks as the grain sizes increased. By contrast, the 650 °C annealed film exhibited drastically reduced absorption in the UV-Vis region owing to its altered crystal structure. These results confirm that the non-annealed, 450 °C annealed, and 550 °C annealed films shared a common bandgap transition mechanism, whereas the 650 °C annealed film underwent crystalline structural reorganization.

The observed discrepancies in absorption intensity originated from the synergistic effects of three interrelated factors: crystal development, microstructural evolution, and phase composition changes. The non-annealed specimen suffered from constrained carrier mobility due to its amorphous and ultrafine-grained structure coupled with a significantly diminished light absorption efficiency owing to the pronounced scattering effects of its rough surface. Annealing at 450 °C initiated preliminary grain growth that enhanced crystallinity and consequently improved the carrier transport ability. Annealing at 550 °C achieved the complete crystallization of the monoclinic $VO_2(M_1)$ phase and produced island-like structures, establishing a dual enhancement mechanism comprising a reduced grain boundary density that minimized carrier scattering and nanostructured islands that amplified mid-infrared absorption through localized surface plasmon resonance effects.[48] When the annealing temperature increased to 650 °C, the formation of the V_2O_5 phase fundamentally altered the band structure of the film, thereby markedly suppressing mid-infrared absorption. This structural evolution reveals the dual sensitivity of VO_2 film optical absorption characteristics to phase purity and nanoarchitecture.

Fig. 2 and 3 present the V 2p and O 1s XPS spectra of the evaluated VO_x films. The V 2p spectrum for VO_2 was deconvoluted into two characteristic peaks corresponding to $2p_{3/2}$ and $2p_{1/2}$.[49] According to the fitting results, the V^{4+} and V^{5+} oxidation states were observed in all specimens. This occurred because the specimens were exposed to air before testing, oxidizing the surface V^{4+} to V^{5+}, which has a higher binding energy. This oxidation was obvious as XPS is a surface-sensitive technology with a detection depth of approximately 1–10 nm. As shown in Fig. 2(a), the non-annealed specimen exhibited a higher proportion of V^{5+} than any annealed specimen. This can be attributed to the amorphous/nanocrystalline structure of the VO_2 film after sputtering, in which the metastable state may

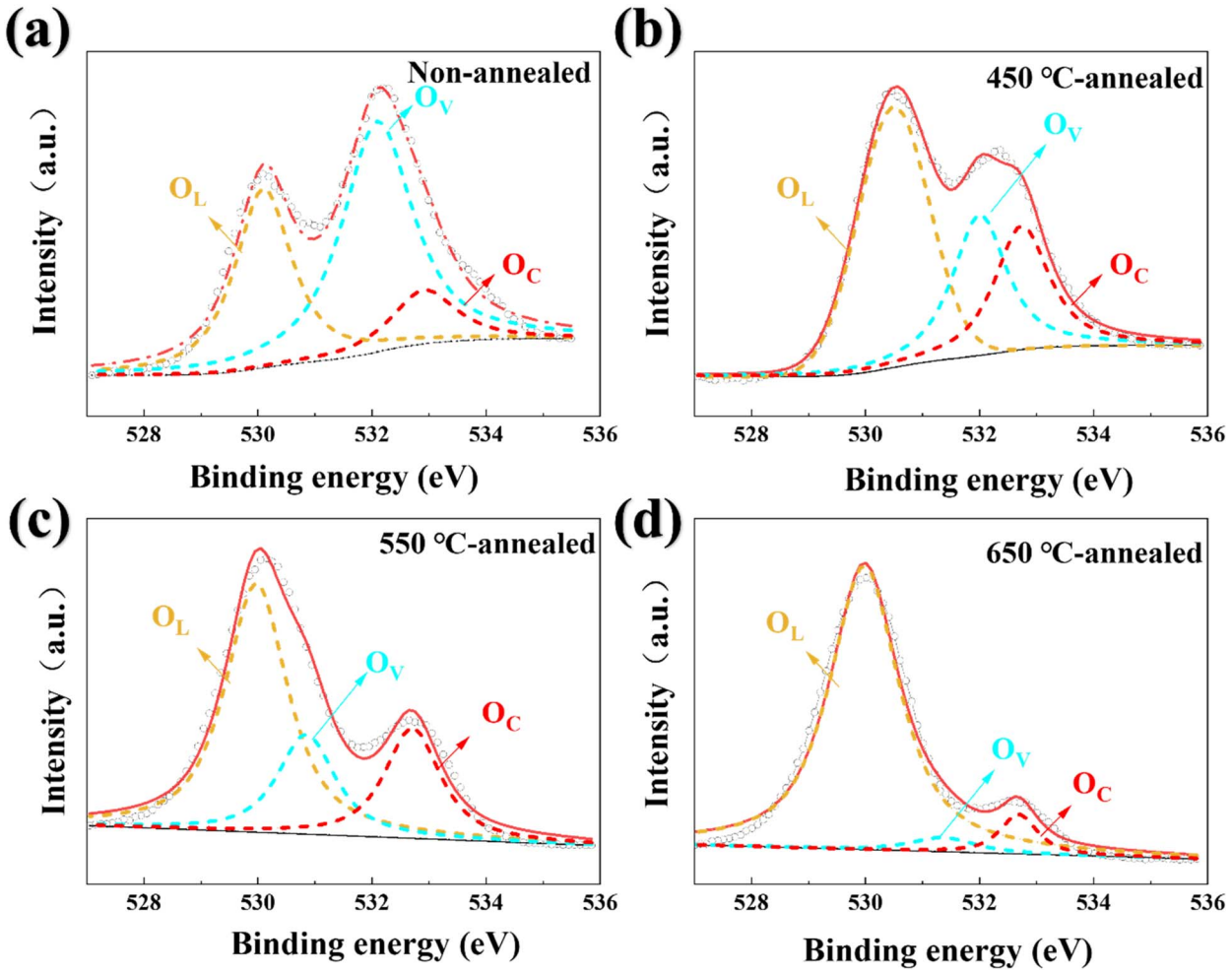

Fig. 3 O 1s XPS patterns of the: (a) non-annealed, (b) 450 °C annealed, (c) 550 °C annealed, and (d) 650 °C annealed VO_2 film specimens.

Table 1 Atomic ratios of O_L, O_V, and O_C obtained from XPS peak-area percentages

Samples	Atomic ratio of O_L	Atomic ratio of O_V	Atomic ratio of O_C
Non-annealed	34.2%	54.1%	11.7%
450 °C-annealed	48.4%	27.3%	24.3%
550 °C-annealed	59.7%	17.3%	23%
650 °C-annealed	75.1%	8.1%	16.8%

contain abundant high-energy defect sites that facilitated the conversion of V^{4+} to V^{5+}. Furthermore, the rough surface of the non-annealed specimen increased the area available for contact with the environment and thereby accelerated surface oxidation. As demonstrated in Fig. 2(b) and (c), vanadium predominantly existed in the lower V^{4+} oxidation state in both the 450 °C and 550 °C annealed specimens, and this state became more dominant as the annealing temperature increased. This dominance can be attributed to annealing-induced grain growth and surface smoothing, which collectively reduced defect density. Concurrently, the flattened surface morphologies of these specimens minimized oxygen permeation pathways, thereby suppressing further oxidation. By contrast, vanadium existed exclusively in the V^{5+} oxidation state with no detectable V^{4+} signals observed when the annealing temperature was 650 °C. This complete valence state transition conclusively confirms the structural phase transformation from $VO_2(M_1)$ to V_2O_5 indicated by the XRD analysis.

The O 1s XPS spectra presented in Fig. 3 further elucidate the effects of the applied annealing temperature on the oxidation state and defect structure of the film. The O 1s core-level XPS spectra exhibited asymmetrical peaks that can be fitted into three components corresponding to lattice oxygen (O_L), hydroxyl groups bonded to metal cations in oxygen-deficient regions (O_V), and chemisorbed or dissociated oxygen from water molecules (O_C).[50]

The non-annealed film (Fig. 3(a)) exhibited the highest proportion of O_V, indicating substantial defects within its amorphous/ultrafine-grained structure, which is consistent with the observed absence of XRD diffraction peaks. This result aligns with the higher proportion of V^{5+} observed in the V 2p spectrum, confirming defect-mediated surface oxidation. The film specimens annealed at 450 °C and 550 °C (Fig. 3(b) and (c))

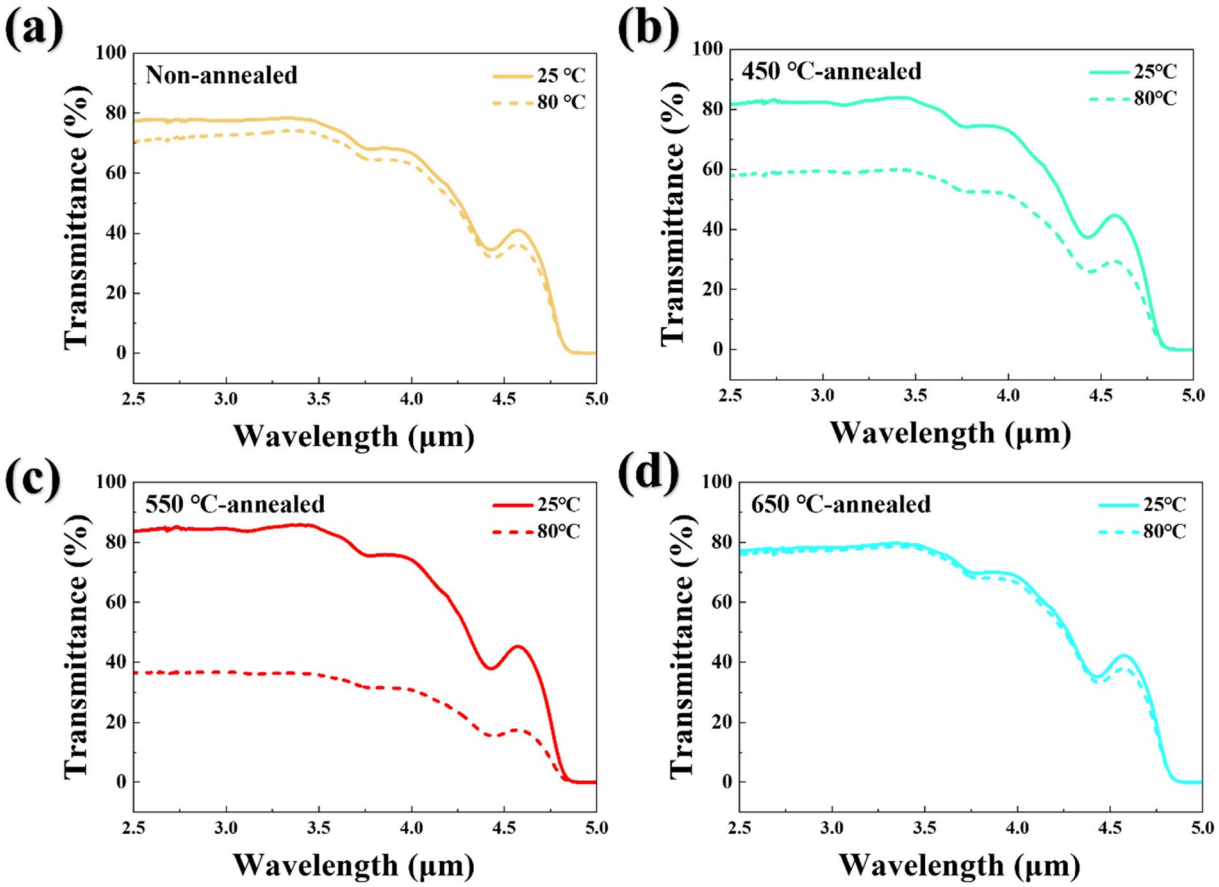

Fig. 4 Optical modulation performance for the: (a) non-annealed, (b) 450 °C annealed, (c) 550 °C annealed, and (d) 650 °C annealed VO_2 film specimens.

exhibited significant increases in the relative intensity of the O_L peak accompanied by substantial reductions in the O_V proportion. This evolution can be attributed to annealing-driven lattice reconstruction in which the crystallization of monoclinic $VO_2(M_1)$ effectively repaired oxygen vacancy defects. Finally, the O 1s XPS pattern of the specimen annealed at 650 °C (Fig. 3(d)) indicates that O_L was even more predominant owing to V_2O_5 recrystallization; this high-temperature annealing process enhanced crystallinity, minimized defects, and formed a low-energy stable surface that suppressed environmental oxygen adsorption.

The peak-area percentages in the O 1s XPS spectra allow the atomic ratios of O_L, O_V, and O_C to be estimated as shown in Table 1. These results provide direct evidence of thermal control over oxygen coordination states through microstructural evolution.

Table 2 Thermal induced mid infrared light modulation performance of vanadium dioxide

Samples	T_0 (before heating)	T_{NL} (after heating)	ΔT (T_0–T_{NL})
Non annealed	76%	72%	4%
450 °C-annealed	82%	59%	23%
550 °C-annealed	85%	35%	50%
650 °C-annealed	78%	77%	1%

3.2 Optical modulation performance

The optical modulation characteristics of the prepared VO_2 thin films in the mid-infrared band were investigated by collecting temperature-dependent transmittance measurements using FTIR (2.5–5 μm) at 25 °C (insulating state) and 80 °C (metallic state); the results are shown in Fig. 4. The non-annealed specimen (Fig. 4(a)) exhibited a modulation depth of only 4% with its transmittance decreasing marginally from 76% at 25 °C to 72% at 80 °C. This minimal response confirms that the amorphous structure of this film fundamentally inhibited effective structural phase transitions. The transmittance of the specimen annealed at 450 °C (Fig. 4(b)) decreased from 82% at 25 °C to 59% at 80 °C, indicating a modulation depth of 23%. Optimal performance was achieved by the specimen annealed at 550 °C (Fig. 4(c)), which exhibited the highest transmittance of 85% at 25 °C with a remarkable reduction to 35% at 80 °C to realize a maximum modulation depth of 50%. This was a combined result of thermally induced structural phase transitions in the highly crystalline VO_2 and enhanced absorption by its uniform island-like grain structure.[32] By contrast, the specimen annealed at 650 °C (Fig. 4(d)) exhibited a negligible difference in

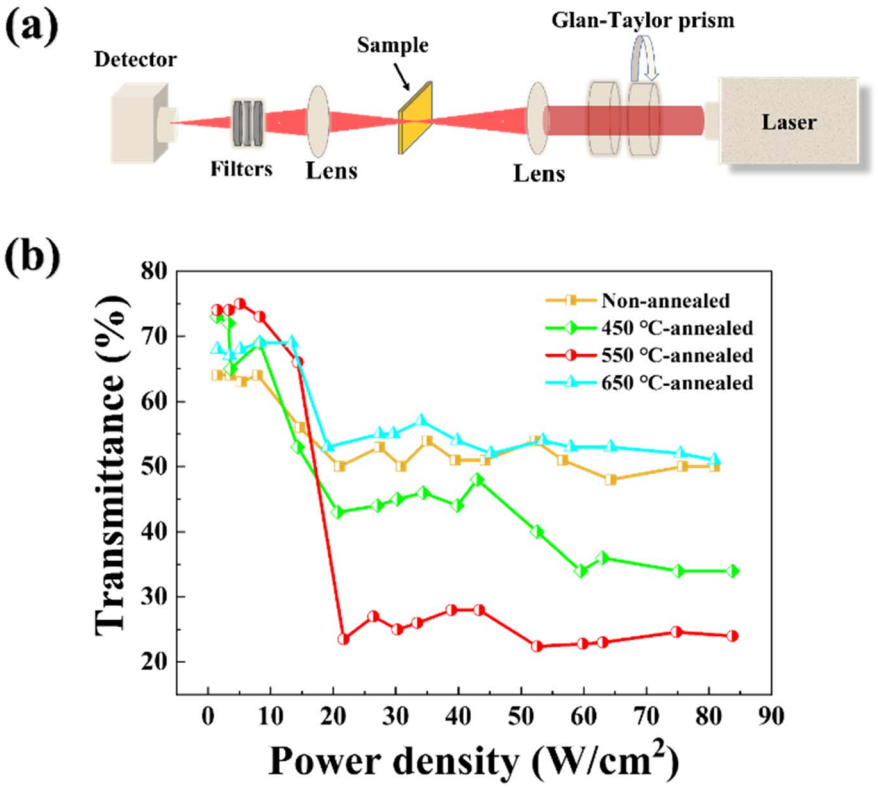

Fig. 5 (a) Schematic of the laser protection efficiency evaluation setup; (b) transmittances of VO_2 films under different laser power densities.

Table 3 Mid-infrared laser (3.8 μm)-induced optical properties of vanadium dioxide

Samples	T_0 (before irradiation)	T_{NL} (after irradiation)	ΔT (T_0–T_{NL})
Non-annealed	64%	50%	14%
450 °C-annealed	73%	34%	40%
550 °C-annealed	74%	24%	50%
650 °C-annealed	68%	51%	17%

transmittance between 25 °C and 80 °C because the film composition was dominated by V_2O_5, which undergoes thermal phase transition at 257 °C. The thermally induced mid-infrared light modulation performance of each VO_2 film is comprehensively described in Table 2. We also tested the optical switching characteristics of these films in the UV-Vis-NIR range (200–2500 nm), and the results exhibited similar trends (Fig. S6).

Laser protection efficiency tests were performed using the custom-built optical limiting test system shown in Fig. 5(a) by applying a 3.8 μm continuous-wave laser with a beam radius of 1 mm and maximum power of 3 W as the irradiation source. Fig. 5(b) presents the measured optical limiting responses. The non-annealed specimen exhibited a transmittance of 64% under low-power irradiation that decreased to 50% when the incident power density increased to 20 W cm^{-2}, corresponding to a modulation depth of 14%; significantly, this is much higher than the 4% modulation depth indicated by temperature-dependent FTIR spectroscopy. This discrepancy originated from the amorphous phase and defective structures, which inhibited effective phase transitions under weak illumination, thereby reducing the overall phase transition efficiency and a weak low-power modulation performance; however, under high-power laser irradiation, the intense power density triggered localized thermal effects, inducing partial phase transitions in specific lattice regions, thereby significantly enhancing the modulation depth.

The transmittance of the specimen annealed at 450 °C was initially high at 73% owing to the annealing-mediated repair of oxygen vacancies and other defects, which effectively reduced the optical scattering and recombination centers present in the non-annealed specimen. When the laser energy density reached 20.7 W cm^{-2}, the specimen transmittance decreased to 43% owing to annealing-induced grain coarsening and increased V^{4+} content. Notably, when the power density increased to approximately 42 W cm^{-2}, the specimen transmittance exhibited a secondary decrease and reached the lowest point of 34% at 59.55 W cm^{-2} for a modulation depth of 39%. This phenomenon was likely caused by laser-driven defect healing in the irradiated regions, where high-power irradiation locally repaired structural imperfections and thereby improved crystalline integrity.

The specimen annealed at 550 °C also exhibited a high initial transmittance of 74% and demonstrated superior optical limiting performance; upon reaching the critical threshold (10 W cm^{-2}), its transmittance plummeted to 28% to realize

Table 4 Infrared modulation performances of VO_2 films fabricated using different methods

Thermally induced				
Irradiation and fabrication method	Transmittance at 25 °C (T_0)	Transmittance at 80 °C (T_{NL})	Transmittance modulation depth ($\Delta T = T_0 - T_{NL}$)	Reference
3–5 μm Al_2O_3 substrate	65%	0.5%	64.5%	51
2–10 μm Si substrate	64.02%	9.94%	54.08%	52
2.5–3.5 μm Quartz substrate 550 °C annealing	85%	35%	50%	This study
Laser-induced				
Irradiation and fabrication method	Transmittance under low-power irradiation (T_0)	Transmittance under high-power irradiation (T_{NL})	Transmittance modulation depth ($\Delta T = T_0 - T_{NL}$)	Reference
3459 nm CW Al_2O_3 substrate	85%	30%	55%	53
3 μm Quartz substrate	77%	18%	59%	54
3.8 μm Quartz substrate 550 °C annealing	74%	24%	50%	This study

a modulation depth of 46%. A secondary decrease in transmittance also occurred in this specimen when the power density reached approximately 42 W cm^2; however, this decrease was only 4%, confirming two key mechanisms: first, high-power laser irradiation partially repaired the residual defects in the irradiated regions; second, the inherent low-defect, highly crystalline structure of the specimen (as indicated by the XRD and XPS results) minimized further defect-mediated losses. Ultimately, this specimen exhibited a total modulation depth of 50%, triple that of the non-annealed specimen.

The sample annealed at 650 °C exhibited an initial transmittance of 68% and an optical limit activation threshold of 13.3 W cm^{-2}, above which it achieved a modulation depth of 17%. This behavior can be primarily attributed to two factors: first, V_2O_5 possesses phase transformation and optical modulation capabilities that were triggered by the thermal energy of high-power laser irradiation; second, large-scale grains coalesced during high-temperature annealing, thereby increasing the overall transmittance by reducing interfacial scattering.

In addition, a thermal imager was incorporated into the test optical path to monitor the temperature at the laser spot in real time. As shown in Fig. S7, the thermal imaging results indicate that during laser irradiation of the sample, the temperature at the center of the laser spot can exceed 400 °C. The high-energy laser not only induces the thermal driven phase transition of VO_x, but also triggers nonlinear absorption mechanisms in the wide-bandgap semiconductor VO_x. As summarized in Table 3, these results demonstrate that the applied annealing temperature governed both the phase transition characteristics and laser-protection performance of the VO_2 thin films through microstructural modification and defect engineering.

The experimental results demonstrated that combining the use of VO_2 targets to mitigate multivalent vanadium interference with subsequent annealing treatment constitutes an effective strategy for fabricating high-performance VO_2 thin films. The comparison of films fabricated using different methods and subjected to different types of laser irradiation in Table 4 indicates that the proposed approach considerably enhanced room-temperature transmittance (85% at 25 °C) under low-intensity illumination while maintaining exceptional suppression of high-power laser irradiation (a 50% modulation depth under 3.8 μm irradiation). Thus, the synergistic optimization of phase purity through stoichiometric sputtering and defect engineering *via* subsequent annealing optimized the trade-off between transparency and laser-limiting efficacy. Clearly, the proposed fabrication method provides a viable technical pathway for developing smart optical protection materials. In the future, based on the present results, combining doping and related processing strategies expected to further optimize the functional performance while maintaining phase stability,[55] thereby enabling broader application prospects.

4 Conclusions

This study successfully achieved the controlled fabrication and laser-protection performance optimization of a $VO_2(M_1)$ thin film by combining magnetron sputtering with subsequent annealing. The optimized film exhibited a 3-fold enhancement in 3.8 μm laser-induced optical modulation depth and a remarkable 12.5-fold improvement in thermally induced mid-infrared modulation depth compared to its non-annealed equivalent. This dramatic improvement can be attributed to the high crystallinity, low-defect surfaces, and uniform island-like morphology of the annealed film. Systematic investigations of the structure–defect–property relationships revealed a tripartite mechanism through which temperature annealing regulates film behavior by: (1) governing the grain size and crystallinity, (2) effectively repairing surface defects, and (3) regulating the valence state transition of vanadium elements.

Finally, the primary factors restricting the use of VO_2 films in optical modulation applications were discussed and the relationships among these factors were clarified. Critically, the results of this study are not only applicable to optical modulation systems but also have reference value for the development of devices such as smart windows and photoelectric switches.

Author contributions

Sen Jin: writing – review & editing, writing – original draft, methodology, investigation. Ningning Dong: writing – review & editing, supervision, project administration. Zhouyuan Yan: investigation. Jincheng Ji: investigation. Weihao Yu: investigation. Jun Wang: resources, funding acquisition.

Conflicts of interest

The authors declare that they have no known competing financial interests or personal relationships that could have appeared to influence the work reported in this paper.

Data availability

Data will be made available on request.

Supplementary information (SI) is available. See DOI: https://doi.org/10.1039/d5ra09458e.

Acknowledgements

This work is supported by the National Key Research and Development Program of China (No. 2024YFA1409400), and the Strategic Priority Research Program of the Chinese Academy of Sciences (Grant No. XDB0890000).

Notes and references

1 K. Wen, X. J. Huang, T. Tian, W. T. Huang and P. G. Liu, *Opt. Express*, 2024, **32**, 5956.
2 Y. Z. Ke, J. M. Xu, J. Ye, J. H. He, J. R. Liang, Y. Zhang, Y. D. Guo, L. Du, J. Y. Leng, P. Zhou and L. Si, *High Power Laser Sci. Eng.*, 2024, **12**, e74.
3 H. Y. Wang, C. G. Ji, C. Zhang, Y. L. Zhang, Z. Zhang, Z. G. Lu, J. B. Tan and L. J. Guo, *ACS Appl. Mater. Interfaces*, 2019, **11**, 11782.
4 S. D. Jackson, *Nat. Photonics*, 2012, **6**, 423.
5 P. Simon, D. Sylvain, A. Chantal and M. Olivier, *Chem. Soc. Rev.*, 2021, **50**, 6613.
6 D. Danilo, C. MJF and H. Michael, *Chem. Rev.*, 2016, **116**, 13043.
7 H. Q. Zheng, L. Zhang, Y. J. Cui and G. D. Qian, *Adv. Photonics*, 2023, **5**, 054001.
8 R. Sabri and H. Mosallaei, *Adv. photonics nexus*, 2023, **2**, 066008.
9 M. J. Zhang, Z. B. Wen, Z. Q. Huang, Y. Z. Chen, M. S. Lin, Y. Shen, Y. Li, S. Y. Yao, Z. Li, Z. Q. Chen and Z. H. Li, *Adv. photonics nexus*, 2024, **3**, 056012.
10 K. Liu, S. Lee, S. Yang, O. Delaire and J. Wu, *Mater. Today*, 2018, **21**, 875.
11 Z. L. Huang, S. H. Chen, C. H. Lv, Y. Huang and J. J. Lai, *Appl. Phys. Lett.*, 2012, **101**, 191905.
12 L. R. Zhao, W. Ou, J. B. Ma, H. J. Zhu, M. Feng and J. C. Liu, *Ceram. Int.*, 2025, **51**, 33619.
13 H. Peng, H. Ping, V. T. Duc, L. Ming, S. C. Wang, Y. J. Ke, X. T. Zeng, L. Q. Mai and Y. Long, *Chem. Rev.*, 2023, **123**, 4353.
14 J. D. Budai, A. Tselev, J. Z. Tischler, E. Strelcov, A. Kolmakov, W. J. Liu, A. Gupta and J. Narayan, *Acta Mater.*, 2013, **61**, 2751.
15 S. Wang, M. Liu, L. Kong, Y. Long, X. Jiang and A. Yu, *Prog. Mater. Sci.*, 2016, **81**, 1.
16 W. Fu, Aerospace Elec, *Countermeasures*, 2002, **1**, 43.
17 C. H. Wan, Z. Zhang, J. Salman, J. King, Y. Z. Xiao, Z. N. Yu, A. Shahsafi, R. Wambold, S. Ramanathan and M. A. Kats, *Laser Photonics Rev.*, 2021, **15**, 2100001.
18 C. H. Wan, E. H. Horak, J. King, J. Salman, Z. Zhang, Y. Zhou, P. Roney, B. Gundlach, S. Ramanathan, R. H. Goldsmith and M. A. Kats, *ACS Photonics*, 2018, **5**, 2688.
19 Z. X. Wang, I. M. Kislyakov, X. Cao, N. N. Dong and J. Wang, *Opt. Lett.*, 2024, **49**, 210.
20 T. C. Chang, X. Cao, N. Li, S. W. Long, Y. Zhu, J. Huang, H. J. Luo and P. Jin, *Matter*, 2019, **1**, 734.
21 L. L. Fan, S. Chen, Z. L. Luo, Q. H. Liu, Y. F. Wu, L. Song, D. X. Ji, P. Wang, W. S. Chu, C. Gao, C. W. Zou and Z. Y. Wu, *Nano Lett.*, 2014, **14**, 4036.
22 J. L. Victor, M. Gaudon, N. Penin, A. Chiron, U. C. Chung, O. Viraphong and A. Rougier, *J. Alloys Compd.*, 2021, **890**, 161890.
23 Y. Lu, C. Q. Zhou, C. Wu and C. W. Zou, *J. Electron. Meas. Instrum.*, 2023, **37**, 179.
24 S. G. Zhao, L. Li, J. L. Zhu, M. L. Liu, T. Zhou, C. Q. Zhou, Z. H. Lin, J. J. Li, B. W. Sun, Y. Lu and C. W. Zou, *Laser Photonics Rev.*, 2024, **18**, 2400426.
25 J. L. Yang, Q. Y. Li, S. Q. Liu, D. B. Fang, J. Y. Zhang, H. B. Jin and J. B. Li, *Adv. Photonics*, 2024, **6**, 046006.
26 Y. Y. Luo, S. S. Pan, S. C. Xu, L. Zhong, H. Wang and G. H. Li, *J. Alloys Compd.*, 2016, **664**, 626.
27 D. P. Zhang, M. D. Zhu, Y. Liu, K. Yang, G. X. Liang, Z. H. Zheng, X. M. Cai and P. Fan, *J. Alloys Compd.*, 2016, **659**, 198.
28 M. Basso, E. Colusso, C. Carraro, C. Kalha, A. A. Riaz, G. Bombardelli, E. Napolitani, Y. Chen, J. Jasieniak, L. E. Ratcliff, P. K. Thakur, T.-L. Lee, A. Regoutz and A. Martucci, *Appl. Surf. Sci.*, 2023, **631**, 157507.
29 R. W. Guo, C. Li, Y. T. Luo, Z. X. Li, F. Lai and J. Li, *Ceram. Int.*, 2024, **50**, 17252.
30 S. A. Bukhari, S. Kumar, P. Kumar, S. P. Gumfekar, H. J. Chung, T. Thundat and A. Goswami, *Appl. Surf. Sci.*, 2020, **529**, 146995.
31 D. Malarde, M. J. Powell, R. Q. Cabrera, R. L. Wilson, C. J. Carmalt, G. Sankar, I. P. Parkin and R. G. Palgrave, *ACS Omega*, 2017, **2**, 1040.
32 E. K. Barimah, D. E. Anagnostou and G. Jose, *AIP Adv.*, 2020, **10**, 065225.

33 E. K. Barimah, A. Boontan, D. P. Steenson and G. Jose, *Sci. Rep.*, 2020, **12**, 11421.
34 T. Kano, H. Nishinaka, Y. Arata and M. Yoshimoto, *Adv. Mater. Interfaces*, 2024, **11**, 2400038.
35 G. Bragaggia, A. Cacciatore, E. Poffe, C. Capone, F. Zorzi, V. Causin and S. Gross, *Molecules*, 2021, **26**, 4513.
36 I. Mjejri, A. Rougier and M. Gaudon, *Inorg. Chem.*, 2017, **56**, 1734.
37 K. L. Gurunatha, S. Sathasivam, J. W. Li, M. Portnoi, I. P. Parkin and I. Papakonstantinou, *Adv. Funct. Mater.*, 2020, **30**, 2005311.
38 Y. F. Gao, H. J. Luo, Z. T. Zhang, L. T. Kang, Z. Chen, J. Du, M. Kanehira and C. X. Cao, *Nano Energy*, 2012, **1**, 221.
39 J. C. Qian, B. Li, S. Q. Tian, B. S. Liu and X. J. Zhao, *Appl. Surf. Sci.*, 2022, **605**, 154680.
40 L. Xiao, H. Ma, J. K. Liu, W. Zhao, Y. Jia, Q. Zhao, K. Liu, Y. Wu, Y. Wei, S. S. Fan and K. L. Jiang, *Nano Lett.*, 2015, **15**, 8365.
41 E. Strelcov, Y. Lilach and A. Kolmakov, *Nano Lett.*, 2009, **9**, 2322.
42 B. J. Kim, Y. W. Lee, B. G. Chae, S. J. Yun, S. Y. Oh, H. T. Kim and Y. S. Lim, *Appl. Phys. Lett.*, 2007, **90**, 023515.
43 K. Abbas, J. Hwang, G. Bae, H. Choi and D. J. Kang, *ACS Appl. Mater. Interfaces*, 2017, **9**, 13571.
44 P. Hu, P. Hu, T. D. Vu, M. Li, S. C. Wang, Y. J. Ke, X. T. Zeng, L. Q. Mai and Y. Long, *Chem. Rev.*, 2023, **123**, 4353.
45 T. K. Le, M. Kang and S. W. Kim, *Mater. Sci. Semicond. Process.*, 2019, **94**, 15.
46 S. Farid, B. Hsu, L. Stan, M. Stroscio and M. Dutta, *Nanotechnology*, 2020, **31**, 095706.
47 D. Gu, Y. T. Li, X. Zhou and Y. Xu, *ACS Appl. Mater. Interfaces*, 2019, **11**, 37617.
48 X. X. Kuai, K. Li, J. M. Chen, H. Wang, J. Y. Yao, C. L. Chiang, T. T. Liu, H. Z. Ye, J. Q. Zhao, Y. G. Lin, L. B. Zhang, V. Nicolosi and L. J. Gao, *ACS Nano*, 2022, **16**, 1502.
49 K. Nishikawa, Y. Kishida, K. Ito, S. I. Tamura and Y. Takeda, *Appl. Phys. Lett.*, 2017, **111**, 193102.
50 J. Mendialdua, R. Casanova and Y. Barbaux, *J. Electron Spectrosc. Relat. Phenom.*, 1995, **71**, 249.
51 S. Wang, P. Chen, Y. Bai, J. H. Yun, G. Liu and L. Wang, *Adv. Mater.*, 2018, **30**, 1800486.
52 K. Xu, Y. Lu, Y. S. Ling and Y. Qiao, *J. Mater. Sci. Eng.*, 2015, **33**, 372.
53 L. Dong, D. W. Zuo and F. XU, *Chem. Eng.*, 2018, **32**, 12.
54 Z. W. Liu, Y. Lu, D. X. Hou and C. W. Zhou, *Chin. J. Lumin.*, 2018, **39**, 942.
55 Y. Q. Wang, G. Yao, Z. J. Huang and Y. Huang, *Acta Phys. Sin.*, 2016, **65**, 057102.
56 A. Boontan, E. K. Barimah and P. Steensonand G Jose, *ACS Appl. Mater. Interfaces*, 2023, **15**, 51606.